



Université
de Paris



Politecnico
di Torino

DISPOSITIFS QUANTIQUES
NANOTECHNOLOGIES FOR ICTs

INTERNSHIP REPORT

Metamaterial for enhanced
light-matter coupling

Internship supervisor:
Prof. Carlo SIRTORI

Candidate:
Marta MASTRANGELO

Academic supervisors:
Prof. Maria Luisa DELLA
ROCCA
Prof. Carlo RICCIARDI

Academic Year 2020/2021

Contents

1	Introduction	3
2	Metamaterial	6
2.1	Patch antenna: state of the art	6
2.2	Patch-antenna resonators for detection	6
2.3	Coupled Mode Theory	8
2.4	Optimization strategies and challenges	10
3	Study of GaAs empty cavity	11
3.1	Reflectivity measurements	11
3.2	Finite Element Method simulations	14
4	2D simulation of a InGaAs/AlInAs QCD	18
4.1	Empty cavity	18
4.2	Cavity filled with the active region	20
4.3	Efficiency and losses	22
5	Conclusions and future perspectives	25
	References	26

Acronyms

CMT	Coupled Mode Theory
FEM	Finite Element Method
FTIR	Fourier-Transform Infrared spectroscopy
FWHM	Full Width Half Maximum
HWHM	Half Width Half Maximum
ISB	Inter Sub-Band
MCT	Mercury Cadmium Telluride
MIR	Mid-Infrared
QCD	Quantum Cascade Detector
QCL	Quantum Cascade Laser
QW	Quantum Well
QWIP	Quantum Well Infrared Photodetector
SEM	Scanning Electron Microscope
TEM	Transmission Electron Microscope

1 Introduction

The internship has been carried out at the Physics Laboratory of the École Normale Supérieure (LPENS), in the group Quantum Physics and Devices (QUAD).

The research activities of the group are oriented toward the development of opto-electronic devices relying on quantum phenomena in materials of reduced dimensionality. In this context, the understanding and control of light-matter interaction at the nanoscale is fundamental: quantum cascade photonics, plasmonics and metamaterials allow the development of innovative optoelectronic devices operating in the infrared and microwave range, thus having a wide field of applications, such as ultra-sensitive infrared detectors, remote sensing and free space communications.

The project presented hereinafter consists in the study of Quantum Cascade Detectors (QCDs) based on patch-antenna metamaterial, both experimentally and via *COMSOL* simulations. Although the technology is already well-established, further investigations are still necessary to optimise the absorption and reduce the spurious photonic losses in the metallic structure that encloses the detector.

First, the absorption properties of GaAs empty cavities have been studied experimentally by measuring the reflectivity spectrum for different geometries to search for an optimal configuration. Then, these results have also been used to optimise the simulations in order to better fit with the non-idealities of the real system, mainly due to the fabrication process. It is possible to go one step further and fill the cavity with a GaInAs/AlInAs heterostructure, which is more interesting both from a physical and a technological standpoint. Being the fabrication procedure the same, the results of the analysis carried out on GaAs cavities can be extended to the simulation of cavities with GaInAs/AlInAs active region. The Finite Element Method simulations performed on these structures will provide a preliminary evaluation before their fabrication and subsequent experimental study. Finally, the long-term goal is to extend this structure to Quantum Cascade Lasers (QCLs), integrating multiple functions in the same device.

Quantum devices The subject of the internship concerns quantum devices operating in the Mid-infrared (MIR) wavelength span ($4 \mu\text{m} < \lambda < 20 \mu\text{m}$). Their peculiarity is that their properties are not constrained to the characteristics of the host material but are controlled by an artificial quantum potential. This is achieved by introducing potential wells in the conduction or valence band, that can be of comparable dimensions with the electron de Broglie wavelengths and therefore induce quantum confinement. In this way it is possible to introduce sub-bands and to exploit the inter-sub-band (ISB) optical transitions for the operation of devices. Such transitions can occur at frequency in the MIR range, since they are no more dependent on the energy gap between the valence and conduction bands, but their energy separation can be engineered by acting on the quantum well design. Also, the selection rules associated to ISBs transitions are different with respect to inter-bands case: only the radiation's component polarized along the growth direction of the heterostructure can be absorbed, so the device has to be designed to match with this requirement.

It is possible to implement photonic detectors based on ISB transitions, such as the Quantum-Well Infrared Photodetector (QWIP) and the Quantum Cascade detector (QCD).

A careful study of the empty resonator is needed to understand the best physical approach to maximise the absorption of the incoming photons and to minimise the losses due to dissipation in the metal or toward the external. Subsequently, the effect of the QW has to be considered in order to assure that the system is able to efficiently convert the absorbed radiation in a photosignal upon the excitation of the ISB transition.

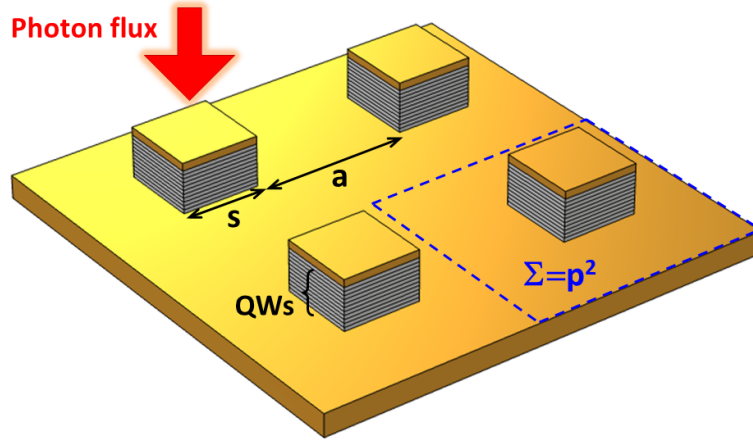


Figure 1.2: Schematic of patch antenna meta-material: it consists in an array of squared double-metal resonators having lateral side s and at distance a . The array periodicity p is given by the sum of s and a and it defines the unit-cell area $\Sigma = p^2$. The resonator is filled with a heterostructure containing the QW where the ISB transition of interest for the QCD operation takes place.

2 Metamaterial

2.1 Patch antenna: state of the art

Photonic metamaterials have allowed the improvement of MIR photonic devices up to room temperature and the development of devices whose properties can be tailored acting on the design of the metamaterial itself. Several structures have been proposed for various scopes, from lasing [2, 3] to detection [4–6], all based on the maximization of light-matter coupling.

In particular, microstrip patch antennas [7] have been extensively used since their first implementation in the 70’s in the Radio Frequency range [8]. Nowadays, they are employed in modern 5G communications technologies owing to their compact size, easy tunability in terms of beam width and polarization and full compatibility with planar fabrication techniques [9].

Recently, arrays of patch antennas acting as microcavities have been obtained by replacing the usual dielectric medium between the two metal plates with a active semiconductor heterostructure. According to the design of such heterostructure, it is possible to implement quantum devices relying on ISB transition exploiting the interaction between the confined electronic states and the cavity confined photonic states [10].

The hybrid nature of these structures combining the antenna and microcavity effect has encouraged the development of different applications. In the THz domain, patch antenna arrays have been used for fundamental studies of the ultrastrong light-matter coupling regime [11, 12], for phase shaping [13] and perfect absorber [14]. Concerning lasing applications, wired antenna arrays represent a monolithic solution to implement THz lasers with high quality factor and low beam divergence, according to the number of resonators constituting the array [3], while the array geometry affects the polarization of the emitted radiation. This device offers excellent flexibility and scalability, for the monolithic architecture does not require complex lithographic processing, nor critical alignment, nor the use of external elements for its operation.

The patch antenna microcavity configuration has already proven to be successful for the realization of MIR detectors, both QWIPs [4] and QCDs [5], preserving high performances up to room temperature. Hereinafter, I will discuss how to apply these photonic structures to further improve the performance of QCDs.

2.2 Patch-antenna resonators for detection

The architecture explored in this work is illustrated in Figure 1.2: it consists in a double-metal square-shaped cavity (patch-antenna) of lateral side s , patterned as an array with inter-patch distance a . The thickness of such cavities has to be much smaller than the wavelength of interest ($2.5 - 25 \mu\text{m}$) to achieve the confinement of the electric field inside the cavity itself. If it is filled with a QCD active region, that is a heterostructure as in Figure 2.1, the resonance of the cavity can be coupled with the ISB transition frequency. The latter depends on the bandstructure design, while the resonant wavelength of the cavities is related to their geometry, and in particular to the lateral patch size s through the equation $\lambda = 2sn_{eff}$, being n_{eff} the modal effective index (depending on the new permittivity introduced by ISB).

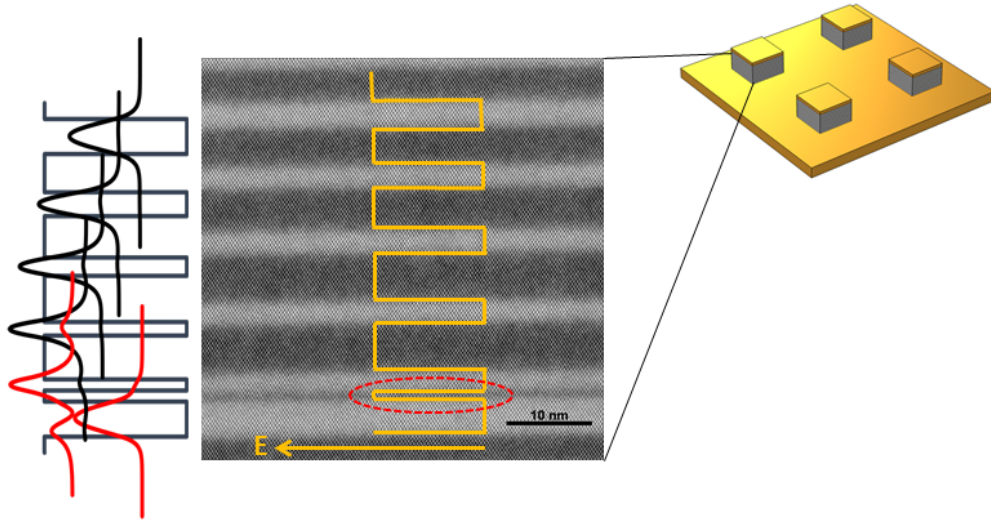


Figure 2.1: TEM image [15] of the heterostructure inserted in the cavity and sketch of its bandstructure [16]. The ISB transition of interest takes place in the narrowest QW, associated to the red wavefunctions, whereas the black ones are associated to the cascade; this arrangement is periodically repeated for a certain number of times, according to the desired thickness of the cavity.

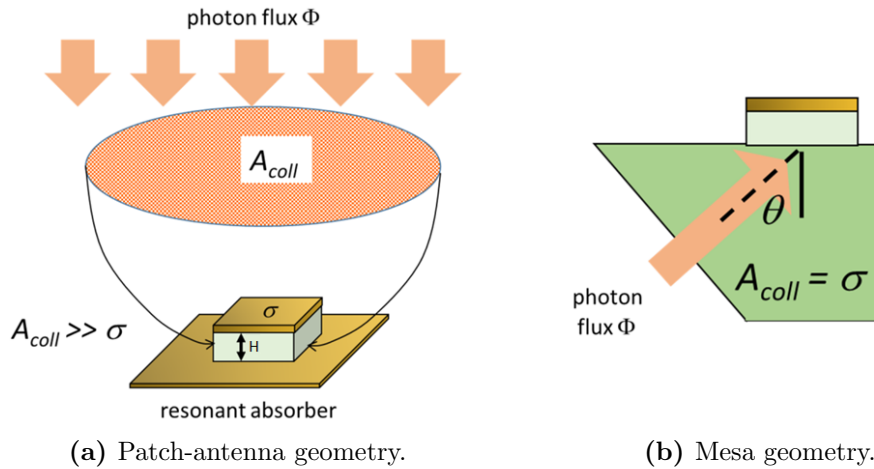


Figure 2.2: Mesa and patch antenna architectures interacting with the incident photon flux [10]: the mesa geometry couples with the external radiation by a 45° facet with the light passing through the substrate before reaching the active region, while the patch-antenna is less sensitive to polarization and normal incident radiation.

Besides the cavity effect enhancing the interaction of the incident electric field and the quantum well, another advantage is that the dark current can be drastically reduced, allowing for room temperature operation. Indeed, such noise current is proportional to the electrical area, that is the areas of the patch resonators $\sigma = s^2$, thus much smaller than the collection area A_{coll} , on which the photocurrent depends. This means that the patch area can be reduced to lower the dark current, yet without affecting the photocurrent because

the antenna effect extends the photon collection area of the detector, as schematised in Figure 2.2a.

Also, this configuration simplifies the light-coupling geometry: with a mesa implementation it is necessary to polish the substrate edge at an angle of a 45° as shown in Figure 2.2b to satisfy the polarization selection rule for the ISB transition, while in the metamaterial this requirement is dropped.

2.3 Coupled Mode Theory

The Coupled Mode Theory (CMT) formalism is ideal to describe the essential features of our system. To this end, it is used to deduce the equations describing the patch-antenna system in order to carry out a valuable optimization strategy.

In this scenario, the resonator (microcavity) and the QW are modeled as two coupled oscillators, whose interaction can be modeled semi-classically. Figure 2.3 offers a schematic representation: the QW is the oscillator on the right, that is a two-level system at frequency ω_p and internal polarization field \mathbf{P} , whereas on the left there is the photonic resonator at frequency ω_a and amplitude field \mathbf{a} . The coupling between the matter excitation and the electromagnetic field occurs through the Rabi frequency Ω_r , defined as [1]:

$$\Omega_r = \sqrt{\frac{\psi^2 e^2}{4\epsilon_0 n_r^2 m^*} f_{12} \frac{N_p n_{2D}}{L}}, \quad (2.1)$$

where n_r is the refractive index, L is the cavity thickness, m^* the effective mass in the QW, n_{2D} is the sheet doping density, f_{12} the oscillator strength of the ISB transition and ψ^2 is the overlap factor of the energy coupled into the z-component of the electric field and overlapping with the semiconductor layers [17]. Therefore, by tuning the doping and the thickness of the absorber it is possible to modify Ω_r , thus the interaction strength between the QW and the patch-antenna.

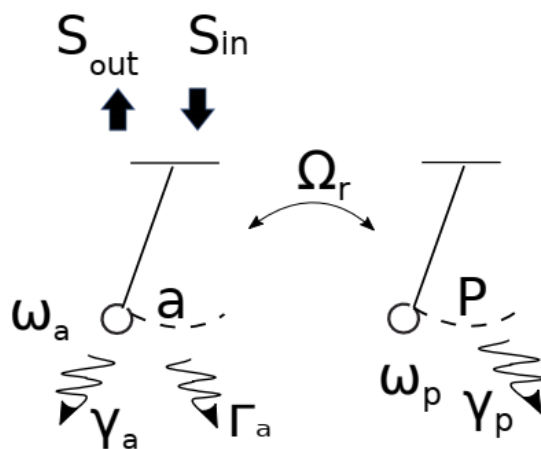


Figure 2.3: Schematic representation of the QW-resonator coupled system [1].

After excitation upon an external radiation \mathbf{S}_{in} , the polarization field decays at a rate γ_p which is the inverse of the lifetime of the excited sub-band in the QW. As only inelastic

and non-dephasing scattering events contribute to the dissipation, a lifetime of 0.5 ps, corresponding to $\gamma_p = 2$ THz, can be assumed. The resonator mode \mathbf{a} can decay either radiatively emitting photons outside the cavity at rate Γ_a or non-radiatively at rate γ_a due to ohmic losses in the metal layers.

Such system is described by the following rate equations [1]:

$$\begin{aligned}\frac{d\mathbf{P}}{dt} &= (i\omega_p - \gamma_p)\mathbf{P} + i\Omega_r\mathbf{a} \\ \frac{d\mathbf{a}}{dt} &= (i\omega_a - \gamma_a - \Gamma_a)\mathbf{P} + i\Omega_r\mathbf{P} + \sqrt{2\Gamma_a}\mathbf{S}_{\text{in}} \\ \mathbf{S}_{\text{out}} &= -\mathbf{S}_{\text{in}} + \sqrt{2\Gamma_a}\mathbf{a}\end{aligned}\tag{2.2}$$

In the case of a monochromatic excitation frequency, they can be solved analytically at the steady state, allowing to compute the key parameters regulating the behaviour of the system.

In the empty cavity case, the model reduces to the case of a single-oscillator, which has to be studied in order to evaluate the best geometry to maximise the absorption and the retention of photons, limiting their dissipation. In this way, once the second oscillator, that is the QW, is inserted in the system, a larger number of photons can be transferred to it, enabling the activation of the ISB transitions needed to generate the photosignal. When studying the single-oscillator case (empty cavity), the desired operating condition is when the absorption rate is equal to the overall losses rate, achieved in the “critical coupling” regime, i.e. $\gamma_a = \Gamma_a$. In this case, the contrast $C = 1 - R$, defined as the complementary of the reflectivity R , reaches 1, meaning that the absorption of the impinging radiation is maximised and no reflection occurs. Hence, when trying to reduce the ohmic losses in gold, it is also necessary to guarantee that radiative losses diminish as well. Increasing the thickness of the cavity is beneficial in terms of non-radiative losses because the modes are less “squeezed” inside the cavity, thus the interaction with the metal layers is less pronounced. On the other hand, radiative losses can be reduced by increasing the periodicity of the patch-antenna array, exploiting the super-radiance phenomenon in which the resonators are coupled via their interaction with the electromagnetic field and display a collective behaviour giving that $\Gamma_a \propto 1/\Sigma$, where $\Sigma = p^2$ is the unit cell area.

When the QW is introduced in the cavity, besides the ability of the system in collecting the impinging radiation, it is meaningful to evaluate also its efficiency in converting it into an electrical signal upon the excitation of the transition in the quantum well. Once the photons have been absorbed in the cavity, they can either be dissipated ohmically in gold (at rate γ_a) or transferred to the QW to activate the ISB transition (at rate Ω_r^2/γ_p). The key parameter regulating this feature is the Rabi frequency Ω_r : when it gets larger, the exchange from the cavity to the QW is increased too. However, if it is increased too much and γ_a becomes negligible, the energy will keep switching back and forth between the two oscillators coherently, so that nothing is released towards the external preventing the extraction of a photosignal.

2.4 Optimization strategies and challenges

The optimization strategy of Quantum Cascade Detectors based on an array of patch antennas is to investigate how the rearrangement of patches can affect their performances. The tuning of the cavity thickness and of the array periodicity can noticeably affect the losses, so it is interesting to observe the improvement obtained when moving toward higher cavities and less dense arrays. Nevertheless, if the distance between patches is remarkably increased, diffraction may arise because p becomes comparable with the operating wavelength. Such phenomenon has already appeared in the Finite Element Method (FEM) simulations that have been performed with different periodicity, so it is interesting to observe how it shows up in the real sample to evaluate the consistency between reality and simulations from this point of view as well.

The final device that I shall simulate is based on an active region made of GaInAs/AlInAs heterostructure. It will be studied through FEM simulations performed for different geometries and optimised using the experimental results obtained on GaAs empty cavity to account for the defects introduced during the fabrication process. The use of GaInAs/AlInAs has several advantages for the unipolar technology, in terms of the physics of the QW and of the marketability of the device. First, it allows to realise much deeper quantum wells, that can accommodate a larger number of sublevels and are suitable for higher ISB transition frequencies. Furthermore, the effective mass of electrons m^* in this structure is lighter, resulting in a larger separation of the sublevels, as the confinement energy is inversely proportional to the mass according to $E = \frac{\hbar^2 k^2}{2m^*}$.

Another key aspect of the heterostructures on InP substrates is that these devices become compatible and fully integrable with the already existing telecom technologies. This feature makes it particularly appealing, both from a market-placement standpoint and for the suitability for being combined with other devices for the realisation of complex optoelectronic systems. The ultimate goal of the patch-antenna QCDs will be to implement these devices with light sources and realise devices for both detection and lasing.

This is the objective of my PhD thesis, in which the conception of the device will be conducted starting from the design of the cavities geometry and of the active region up to the fabrication and characterization of the device.

3 Study of GaAs empty cavity

The first step in the implementation of patch-antenna structure on detectors is to investigate the properties of the empty cavity. This will be the starting point for the bandstructure design, in order to make the best coupling between the QW and the cavity mode. Indeed, this meta-material architecture relies on matching the resonance of the cavity with the ISB transition, so investigating the feature of the cavity is the preliminary step to do before introducing the active region where the ISB transition will take place.

3.1 Reflectivity measurements

The structures under study are patch-antenna arrays as the one displayed in Figure 3.1, where it is shown a picture taken with the Scanning Electron Microscope of an array with period $p = 6.5 \mu\text{m}$ and patches with lateral side $s = 1.37 \mu\text{m}$ and thickness $H = 500 \text{ nm}$.

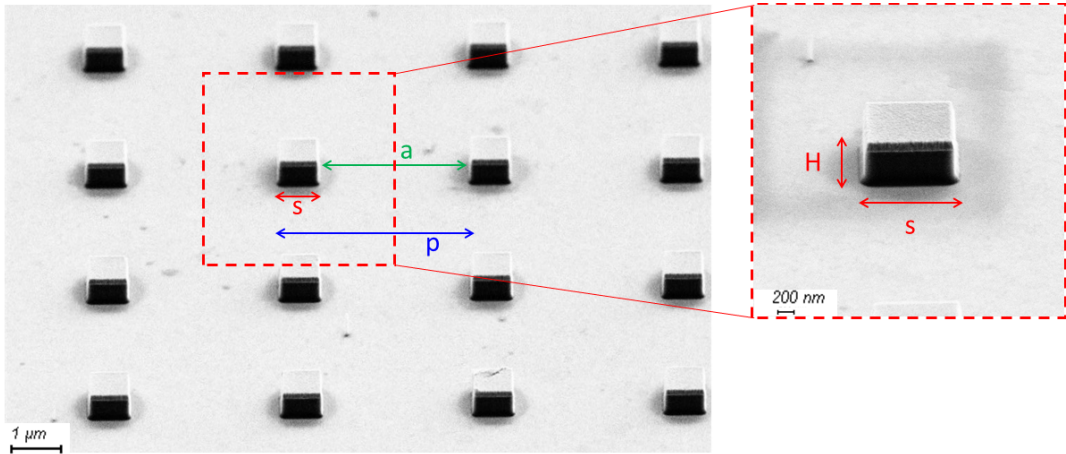


Figure 3.1: SEM image of the patch antenna array ($s = 1.37 \mu\text{m}$, $p = 6.5 \mu\text{m}$, $H = 500 \text{ nm}$) and zoom on the single patch.

The measurements have been performed on arrays with different periods ($3 \mu\text{m}/4.5 \mu\text{m}/5.5 \mu\text{m}/6.5 \mu\text{m}/10 \mu\text{m}/14 \mu\text{m}/18 \mu\text{m}$) and cavity heights ($500 \text{ nm}/1600 \text{ nm}$), while s is kept equal. Consequently, the resonance frequency is expected to be $\sim 35 \text{ THz}$ for all of them, according to

$$f_{res} = \frac{c}{\lambda} = \frac{c}{2sn_{GaAs}}. \quad (3.1)$$

At this frequency the absorption in the cavity is expected to be maximised, corresponding to a dip in the reflectivity spectrum. The following analysis aims to verify how the contrast and the features of such peaks are modified at the varying of the period p .

In order to evaluate the absorption properties of the GaAs cavities, their reflectivity has been measured using the setup depicted in Figure 3.2. The impinging beam coming from a FTIR spectrometer is a collimated black body radiation (at 1153 K) which is sent to a concave mirror that focuses it on the sample, rotated of 45° to deflect the radiation

toward a second concave mirror. Here, the light will exit collimated; so, before arriving to the MCT detector, a third concave mirror is needed in order to focus the beam.

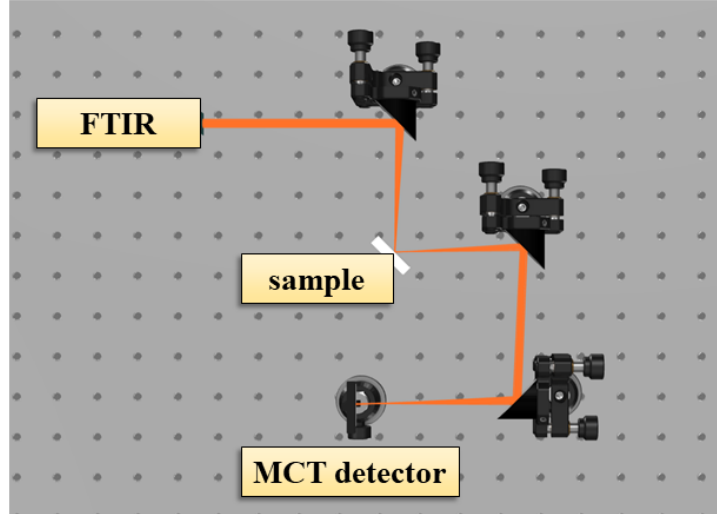


Figure 3.2: Optic setup for reflectivity characterization.

Since the measurement is not performed in vacuum conditions, atmospheric absorption has to be considered. For this reason, the gold substrate where the cavity arrays are placed is taken as reference to calibrate the black body spectrum with respect to the absorption not related to the microcavity. Specifically, both the spectrum of the signals reflected by the cavity and by the sole gold are measured and then the former is divided by the latter. After applying a baseline correction to the normalised curve, the reflectivity spectra shown in Figure 3.3 are obtained. The results reported here refer to an array of patches having thickness 500 nm and different periods (3 μm /4.5 μm /5.5 μm /6.5 μm /10 μm /14 μm /18 μm), so that one can appreciate the effect on the features of the absorption peak. Also, it is possible to see that diffraction introduces a second peak that gets closer and closer to the resonance frequency when p is increased.

Even if it remains centered in the same resonance frequency (35 THz), the shape of the absorption peak is modified, becoming narrower and deeper when p is increased. Figure 3.4 summarises these trends; it has been obtained by extracting from the reflectivity spectra the values of the contrast C and the Full Width Half Maximum (FWHM) of the Lorentzian fitting the experimental curve (see the inset of Figure 3.3) which is related to the overall losses rate $\Gamma = \gamma_a + \Gamma_a$ according to $\Gamma = \text{FWHM}/2 = \text{HWHM}$.

Thanks to the CMT, it is possible to evaluate the losses rates: from the rate equations (eq.2.2), it can be derived the system that has to be solved in order to find radiative and non-radiative losses [1]:

$$\begin{cases} C = \frac{4\gamma_a\Gamma_a}{(\gamma_a + \Gamma_a)^2} \\ \Gamma = \gamma_a + \Gamma_a \end{cases} \quad (3.2)$$

The values of C and Γ have to be retrieved from the reflectivity spectra, so that it is

possible to compute the losses as:

$$\begin{cases} \gamma_a = \frac{\Gamma}{2}(1 - \sqrt{1 - C}) \\ \Gamma_a = \frac{\Gamma}{2}(1 + \sqrt{1 - C}) \end{cases} \quad (3.3)$$

Figure 3.5 reports the results of the calculations. It is clearly noticeable that the non-radiative losses are smaller in the thicker cavity, meaning that the overlap between the gold layers and the evanescent wave of the confined mode, responsible for ohmic dissipation, is less substantial when the height is increased. It is also noticeable that when p gets larger the radiative losses decrease thanks to super-radiance ($\Gamma_a \propto 1/p^2$), whereas the non-radiative ones become larger. Hence, looking at the behaviour of the losses rate allows one to study when the critical coupling regime ($\gamma_a = \Gamma_a$) is reached. When $H = 500$ nm (Figure 3.5a), this condition is achieved for p between $6.5 \mu\text{m}$ and $10 \mu\text{m}$, while for $H = 1600$ nm (Figure 3.5b) a larger period is needed. If p is further increased after the entrance in the critical coupling, the non-radiative losses will overcome the radiative ones and the contrast will decrease as one can see in Figure 3.4.

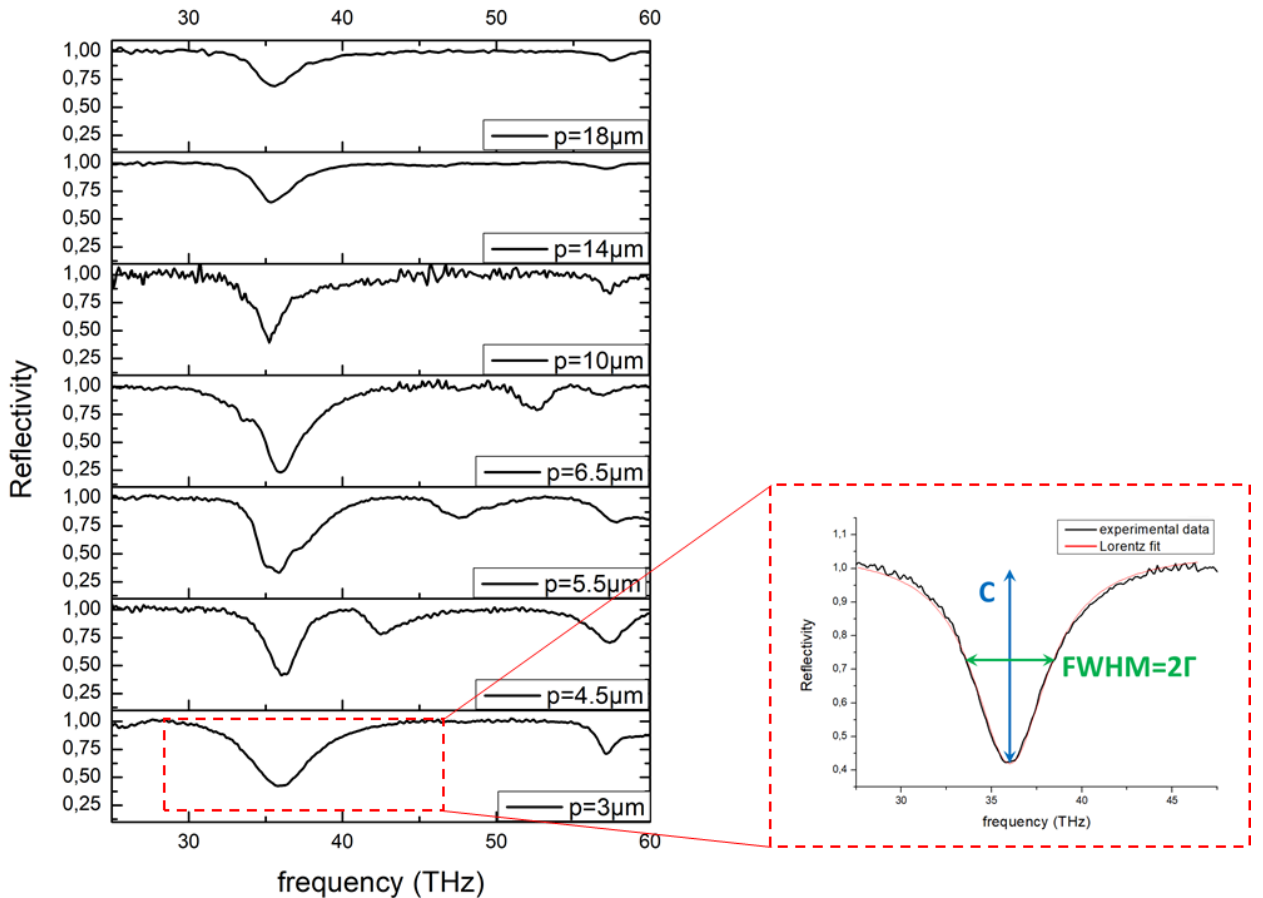


Figure 3.3: Normalised reflectivity spectra with baseline correction for different periods. The inset shows the definition of the contrast C and the total losses Γ , the latter being related to the FWHM of the Lorentzian fitting function of the absorption peak ($\Gamma = \text{FWHM}/2$).

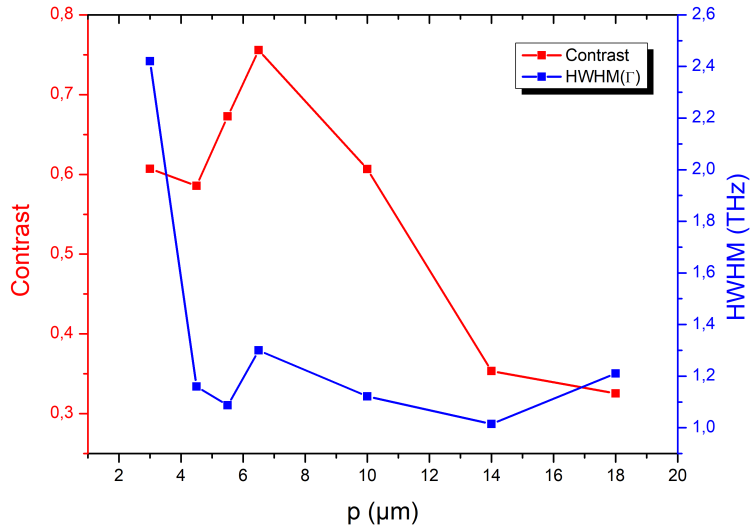
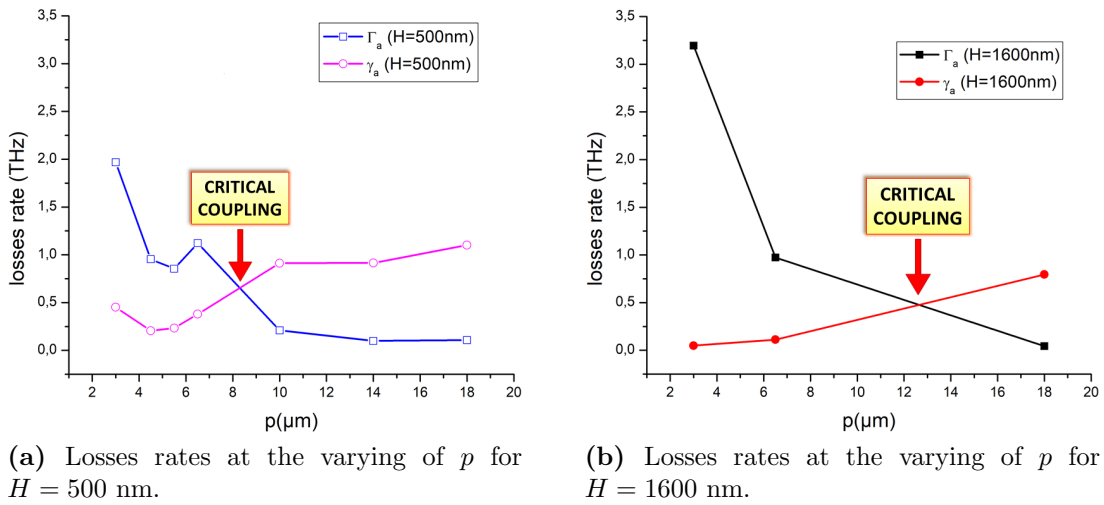


Figure 3.4: Contrast and HWHM of the absorption peak at the varying of p ($H = 500$ nm) extracted from the reflectivity spectra.



(a) Losses rates at the varying of p for $H = 500$ nm.

(b) Losses rates at the varying of p for $H = 1600$ nm.

Figure 3.5: Losses rates at the varying of p derived from CMT with the experimental reflectivity spectra for different heights of the cavity.

3.2 Finite Element Method simulations

Finite Element Method (FEM) simulations are a valuable tool in order to study and predict the behaviour of a system. They have been conducted in 2D via *COMSOL Multiphysics*. In order to account for the array-like organization of the patches, Floquet boundary conditions have been imposed. In this way, it is possible to focus the analysis on the schematic depicted in Figure 3.6, which will be repeated infinitely many times to simulate an array of infinite size. The metal layers at the top and the bottom acting as cavity and antenna are in gold, while the internal of the cavity is in GaAs.

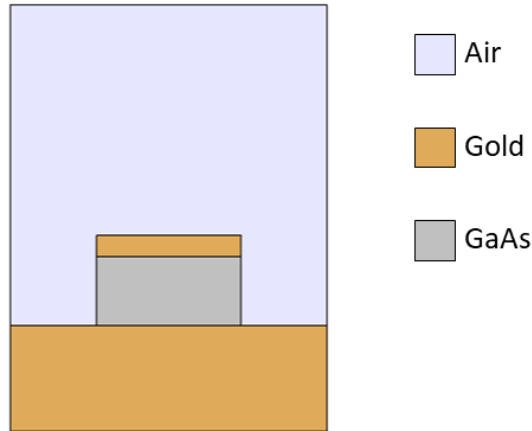


Figure 3.6: 2D schematic of the empty cavity simulated via COMSOL.

At first, the refractive index to use in the simulations have been taken from literature, both for GaAs [18] and gold [19]. Then, in order to get a good agreement with the experimental results, it is necessary to account for non-idealities due to the fabrication process that can increase the ohmic losses, inducing a deviation from the expected behaviour. One of this is related to the fact that the Au top contact does not have the characteristic values found in the literature [19], but there is a discrepancy due to the many impurities present and to the deposition of a layer of Pd/Ge/Ti/Au (rather than plain Au) to improve the adhesion. It is possible to account for this issue in the simulations by tuning the parameter γ_{bulk} , associated to scattering, in the expression of the Drude-like dielectric function of gold [20]:

$$\epsilon_{Au}(\omega) = 1 - \frac{\omega_p^2}{\omega^2 + i\gamma_{bulk}\omega_p}, \quad (3.4)$$

where ω_p is the plasma frequency, here set to be 13697 rad/s [21].

The adequate value for γ_{bulk} can be estimated by comparing the simulation with the experimental results, using it as a fitting parameter. It is worth to remark that the results from the experimental characterization of the empty cavities can be straightforwardly extended to different materials, as long as the fabrication process is the same.

Once the parameters for the simulation have been defined coherently with the real physical system, it can be studied the adherence of the FE analysis with the experimental results discussed above. Figure 3.7 shows the comparison between the reflectivity spectra found experimentally and via COMSOL simulations for different periods $p = 3 \mu\text{m}/4.5 \mu\text{m}/5.5 \mu\text{m}/6.5 \mu\text{m}/18 \mu\text{m}$ and $H = 500 \text{ nm}$.

The agreement between simulations and experimental results is reasonable: the peak is centered at 35 THz as expected considering the lateral side s and the contrast is improved for larger periods. Nevertheless, while the experimental analysis has shown that the contrast is maximised when p is between $6.5 \mu\text{m}$ and $10 \mu\text{m}$, in the simulations its trend is always improved up to $p = 18 \mu\text{m}$. This feature matches with the losses rates computed following the procedure explained in sec.3.1 and depicted in Figure 3.8. Indeed, while the radiative losses rates evaluated using the experimental and the simulations results exhibit a very similar behaviour, that is proportional to $1/p^2$, for the non-radiative ones it is not

the case. In particular, the experimental curve shows an increase that eventually allows to enter the critical coupling regime. On the other hand, the FEM simulations give a flat trend for which it is necessary to have a larger periodicity before satisfying the condition $\gamma_a = \Gamma_a$, that is the critical coupling.

This discrepancy can be ascribed to several factors: besides the fact that simulations are performed in 2D, there are many different non-idealities that cannot be predicted and included. They may be due to the disorder and the impurity of the materials that act as scattering centers, as well as the fabrication process that can give not perfectly homogeneous patches. Also, even if the correction of the gold dielectric function through the fitting parameter γ_{bulk} allows to build a model closer to reality, the Pd/Ge/Ti/Au layer introduces such a complexity that cannot be included in the simulation.

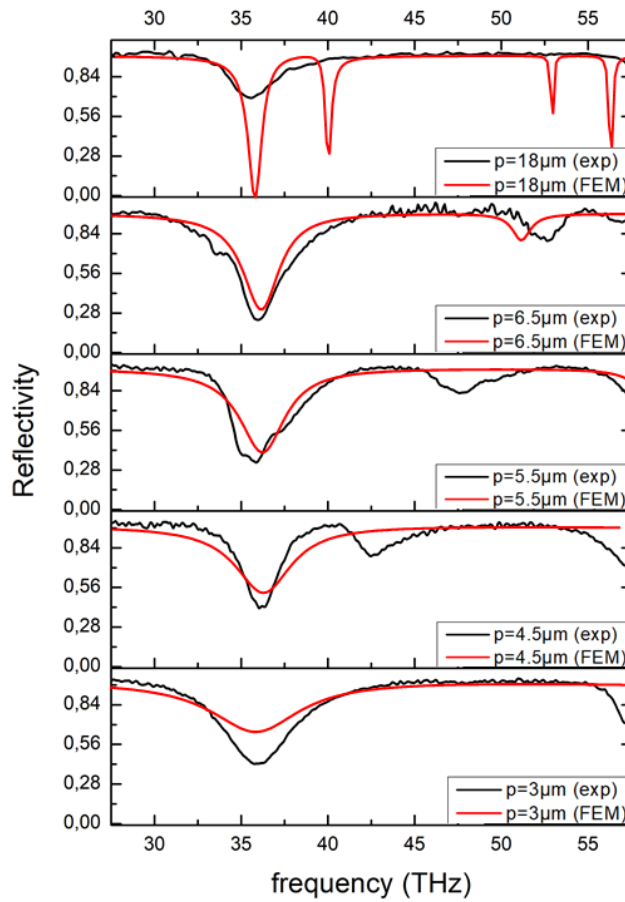


Figure 3.7: Reflectivity spectra at different p ($H = 500$ nm) obtained experimentally and via COMSOL simulations.

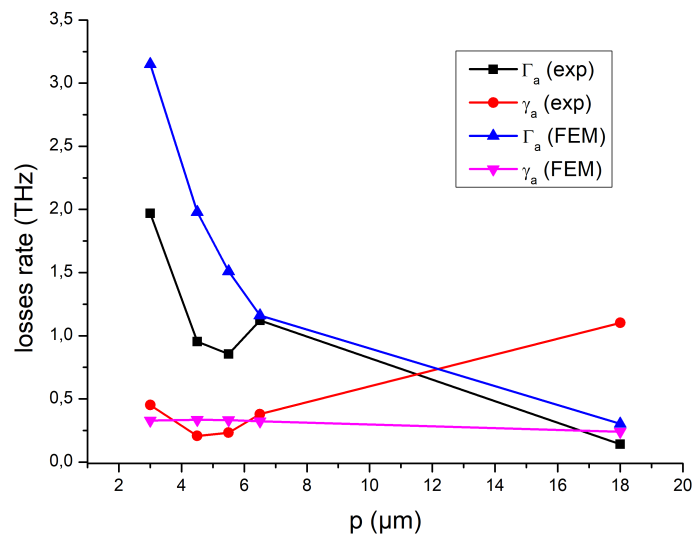


Figure 3.8: Losses rates at different p ($H = 500$ nm) obtained experimentally and via COMSOL simulations.

4 2D simulation of a InGaAs/AlInAs QCD

The FEM analysis has been carried out also on a Quantum Cascade Detector in GaInAs/AlInAs designed to operate at a wavelength of 9 μm , corresponding to a frequency of about 33 THz.

The schematic used in this case, depicted in Figure 4.1, is similar to the one used for the empty GaAs cavity but for the presence of the active region filling the cavity and the highly doped contact layers (Si, 10^{18}cm^{-3}). Its thickness is 850 nm, so that the size of the cavity is much smaller than the operating wavelength to provide an effective sub-wavelength confinement. The cavity is modeled by repeating for 19 periods the structure on the right of Figure 4.1, that is a InGaAs “quantum-well” layer followed by a “cascade” layer. The properties of the latter have been set by computing an effective complex refractive index as a weighted average between InGaAs and AlInAs, according to the thickness of the wells and barriers in the cascade. Concerning the QW layer, its refractive index has been adjusted to fit either the empty or filled cavity case. The former allows to analyse the properties of the empty cavity and its resonance, while the latter allows to include the effects of ISBs transition occurring in the quantum well that will couple with the cavity, enhancing its response when their resonance frequencies coincide.

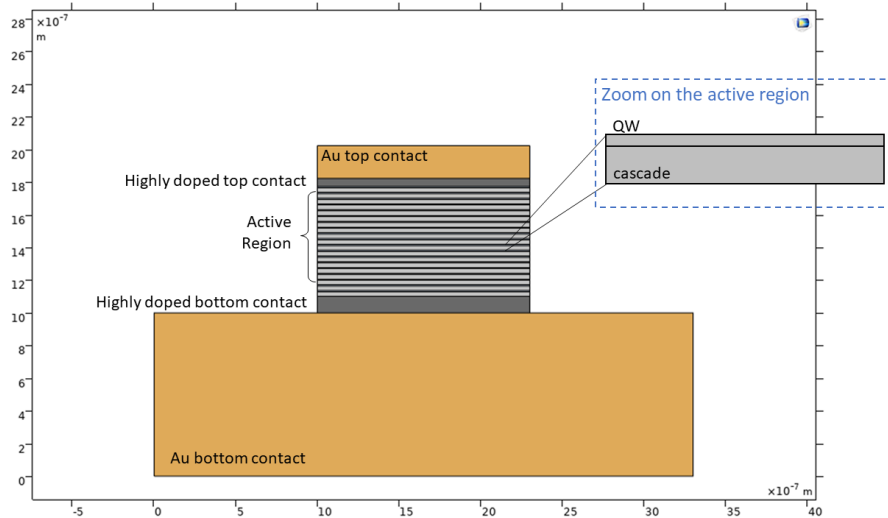


Figure 4.1: 2D schematic of the patch and zoom on the active region simulated via COMSOL. Below the double-metal Au layer there are the highly doped (Si, 10^{18}cm^{-3}) GaInAs contact layers and the GaInAs/AlInAs active region, modeled as an alternation of QW and “cascade” layers, is sandwiched between the two.

4.1 Empty cavity

First, the properties of the empty cavity have been investigated. Here, the refractive index of the quantum well layer has been set as isotropic using the values in the literature [18]. Concerning gold, the values of γ_{bulk} found for GaAs empty cavity has been used to evaluate the dielectric function in equation 3.4 and the simulations have been run using the refractive index computed in this way. Even if the defects introduced in the fabrication

process are expected to be very similar to GaAs cavities, in the real structure there are other factors that generate disordered features acting as source of scattering and therefore producing optical losses. Therefore, there will never be a full adherence of experiments with simulation and a final optimization will be needed upon the characterization of the real device.

In order to optimise the design, the behaviour of the patch has been simulated for different values of the lateral size s to find the value that allows to match with the frequency of interest. The behaviour of the resonance with respect to $1/s$ is linear, revealing a blue-shift toward higher frequencies for smaller s , as summarised in Figure 4.2. The lateral side best matching with the 9 μm requirement is 1.3 μm , so it is set to this value in the following simulations, performed by varying p in order to optimise the contrast. As one can see in Figure 4.3, the resonance ~ 33 THz is achieved for different values of p , but the contrast is improved at larger periods, even if diffraction becomes visible at $p = 7.5$ μm .

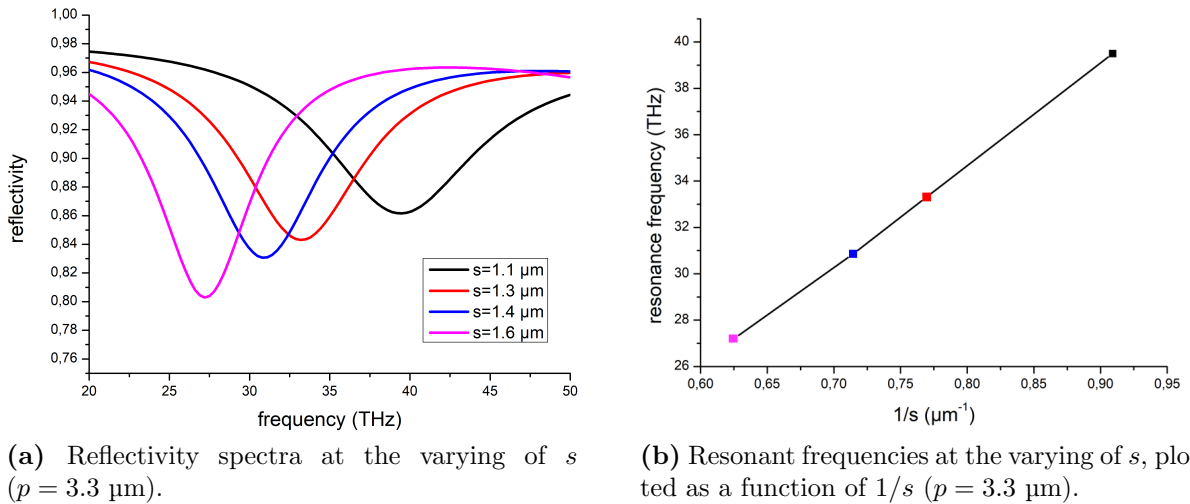


Figure 4.2: Reflectivity and resonance frequency in the empty cavity for different values of the lateral patch size s .

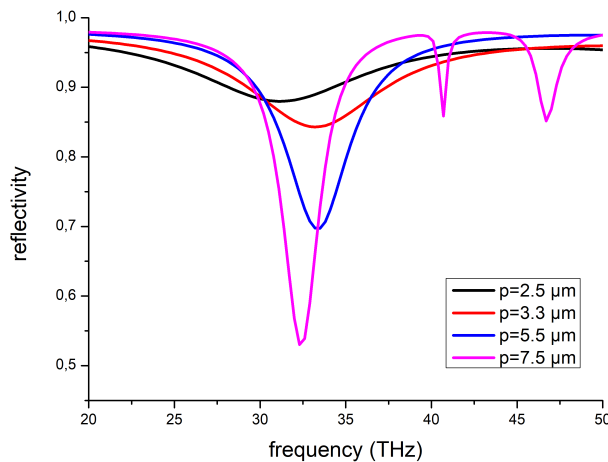


Figure 4.3: Reflectivity spectra at the varying of p ($s = 1.3$ μm).

4.2 Cavity filled with the active region

Once the properties of the empty cavity have been investigated, the effect of the quantum well has to be included in order to verify the coupling of the two. This can be introduced by modifying the refractive index of the QW region by setting an anisotropic refractive index in order to account for the ISB transitions along the direction transverse to the plane where radiation impinges. Indeed, the presence of the quantum well will affect only one spatial direction, that is only one component of the complex refractive index. The values used in the simulations both for the transverse and in-plane components have been found by using a Matlab script developed by the QUAD group. It takes as inputs the parameters obtained with the evaluation of the bandstructure, simulated by using a specific Software able to compute it for a given heterostructure. In particular, the relevant features for the QW refractive index are the characteristics of the well (doping and thickness), the amplitude and the oscillator strength associated to the transition, and the damping factor. Then, the in-plane and transverse components of the refractive index are given as output, so that they can be used in COMSOL to define a tensor which preserves the same value of the empty cavity along the directions not affected by the QW, and the new value (shown in Figure 4.4) for the transverse direction. In the curves it is visible the effect of the QW that introduces a resonance at 33 THz, that is the transition frequency.

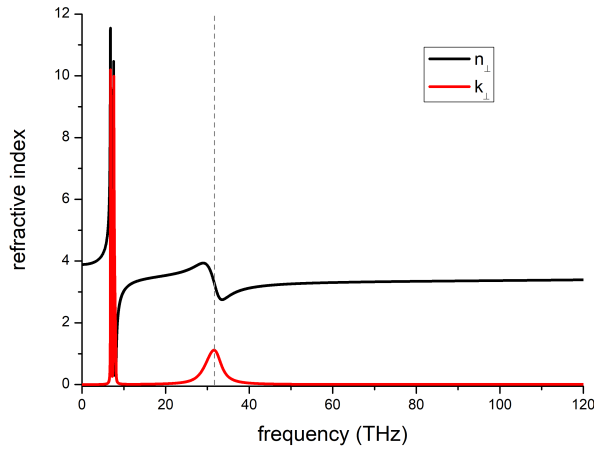
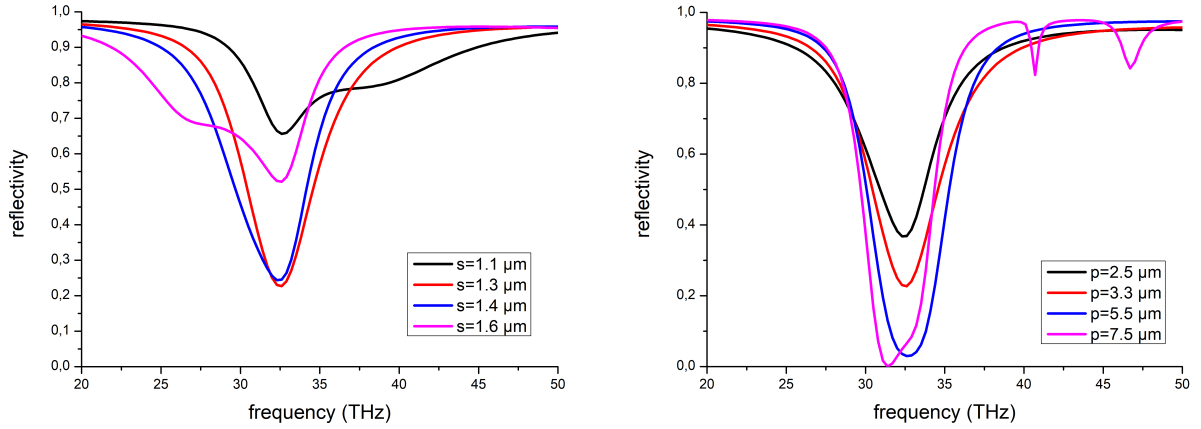


Figure 4.4: Transverse component of the real and imaginary part of the refractive index along the transverse direction. The resonance is visible in correspondence of 33 THz, indicated by the grey dashed line.

In this way it is possible to study how the QW modifies the absorption of the empty cavity. In particular, in the reflectivity curve depicted in Figure 4.5a it is possible to notice the presence of the QW that introduces an absorption peak beyond the one of the cavity. When the two peaks are at the same frequency (at $s = 1.3 \mu\text{m}$), the resonance condition is achieved, resulting in the enhancement of the absorption. When s is set to a value that drives the cavity mode farther than the ISB transition, the coupling between the two is no more effective. After having fixed s to the proper value to have the resonance, the simulation is run for different values of p , obtaining the result in Figure 4.5b. When modifying p , a slight shift of the resonance may occur, so it is always necessary

to double-check to have the correct matching with the cavity mode, eventually correcting s if necessary. Concerning the contrast, it is improved for larger periods as expected, but diffraction becomes visible when p is increased up to a value comparable with the operating wavelength of $9 \mu\text{m}$.



(a) Reflectivity at the varying of s ($p = 3.3 \mu\text{m}$). (b) Reflectivity at the varying of p ($s = 1.3 \mu\text{m}$).

Figure 4.5: Reflectivity in the full cavity for different values of s and p .

Finally, in order to appreciate the effectiveness of the coupling between the cavity and the QW, it is worth to look at the comparison of the reflectivity spectra at $s = 1.3 \mu\text{m}$ between the full and empty cases, depicted in Figure 4.6. Here, it is possible to verify that at $p = 3.3 \mu\text{m}$ the contrast, thus the absorption, is significantly improved without worsening the peak shape.

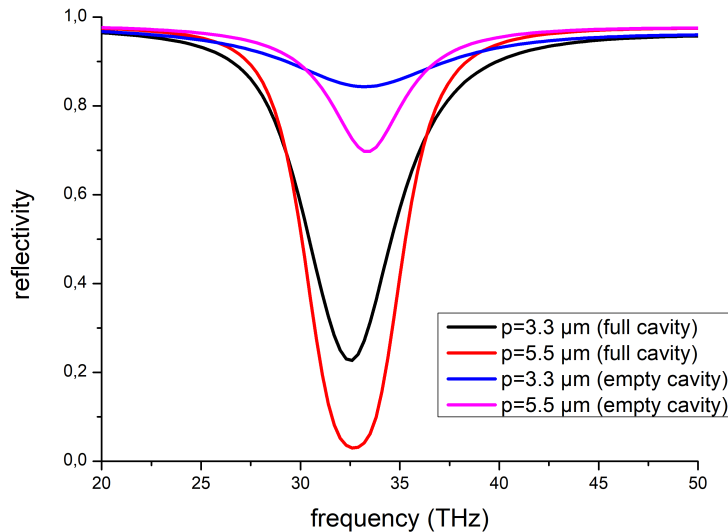


Figure 4.6: Comparison of the reflectivity in the empty and full cavity ($s = 1.3 \mu\text{m}$).

4.3 Efficiency and losses

A key parameter to study the quality of the simulated architecture is the absorption quantum efficiency, defined as the ratio between the number of photons absorbed in the optical transition and the incoming number of photons. Such feature is fundamental for a detector, since it quantifies the ability of the system in absorbing the impinging radiation. The efficiency can be numerically evaluated: the value of the input power P_{in} is set at the beginning of the simulation, while the absorbed power can be computed using the obtained results. Starting from the expression of the absorbed power density [22]:

$$p_a = \frac{\omega}{2} \operatorname{Re}\{j\epsilon\} |E|^2 = \frac{2\pi f}{2} \epsilon_0 (2nk) |E|^2, \quad (4.1)$$

the overall absorbed power in the quantum well can be computed integrating over the total QWs surface. It is remarkable that due to the ISB selection rules, only the transverse component of the electric field E_{\perp} can be absorbed, so one obtains:

$$P_a = 2\pi f \epsilon_0 n(f) k(f) \int_{QW} |E_{\perp}|^2 dS, \quad (4.2)$$

where f is the frequency and ϵ_0 is the vacuum permittivity.

Finally, the absorption efficiency will be given by the ratio $\eta = P_a/P_{in}$, evaluated at the resonance frequency. One can study how η is modified for different values of s and p , comparing the results obtained evaluating the equation 4.2 at the resonance frequency, as reported in Figure 4.8.

It is also possible to evaluate the spatial evolution of the efficiency in the whole structure since it is proportional to the absorbed power density p_a . Figure 4.7 displays the profile obtained evaluating equation 4.1 at $s = 1.3 \mu\text{m}$ and $p = 3.3 \mu\text{m}$, showing that the absorption is maximised in the QWs.

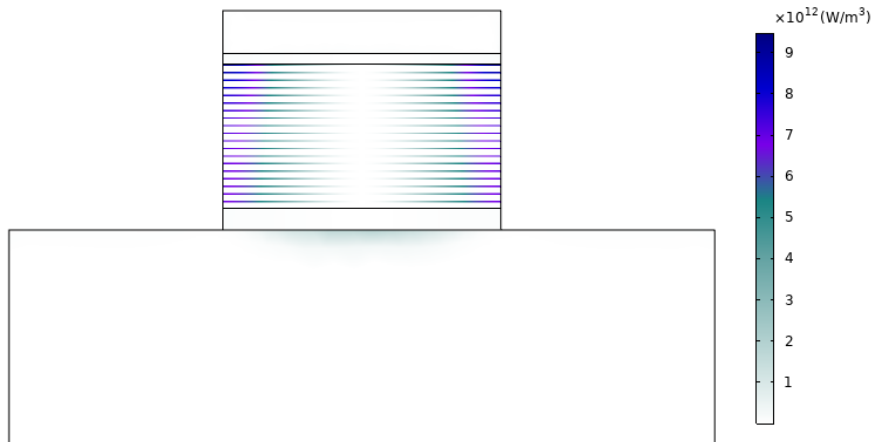


Figure 4.7: Spatial distribution of $\eta \propto p_a$ at $s = 1.3 \mu\text{m}$ and $p = 3.3 \mu\text{m}$.

The study on the efficiency can be completed using the Coupled Mode Theory (CMT) as well. Assuming a monochromatic excitation $\mathbf{S}_{in} = S_0 e^{i\omega t}$, equations 2.2 can be analytically solved for the steady state. In this way, it is possible to evaluate the absorption

efficiency, defined as:

$$\eta_{CMT} = \frac{2\gamma_p |\mathbf{P}|^2}{|\mathbf{S}_{in}|^2}, \quad (4.3)$$

that is the intensity absorbed by the cavity (excluding the ohmic losses) over the incident intensity. Substituting in the above formula the expression of \mathbf{P} obtained solving the rate equations, one gets:

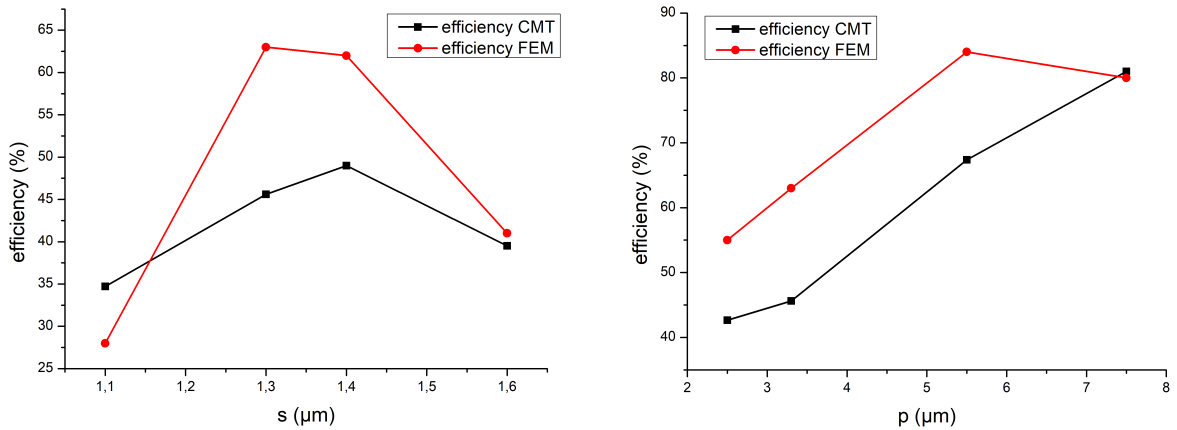
$$\eta_{CMT}(\omega) = \frac{4\gamma_p \Gamma_a \Omega_r^2}{[\gamma_p(\omega - \omega_a) + (\gamma_a + \Gamma_a)(\omega - \omega_p)]^2 + [\gamma_p(\gamma_a + \Gamma_a) + \Omega_r^2 - (\omega - \omega_a)(\omega - \omega_p)]^2}$$

that simplifies to:

$$\eta_{CMT}^{max} = \frac{4\gamma_p \Gamma_a \Omega_r^2}{\gamma_p(\gamma_a + \Gamma_a) + \Omega_r^2} \quad (4.4)$$

when evaluated at the resonance and $\omega_a = \omega_p (= \omega)$.

Then, one can proceed with the evaluation of the efficiency inserting the values for the losses rates obtained through eq. 3.3 in eq. 4.4 and assuming $\gamma_p = 2$ THz and $\Omega_r = 1.2$ THz; the results are reported in Figure 4.8.



(a) Efficiency at the varying of s ($p = 3.3 \mu\text{m}$).

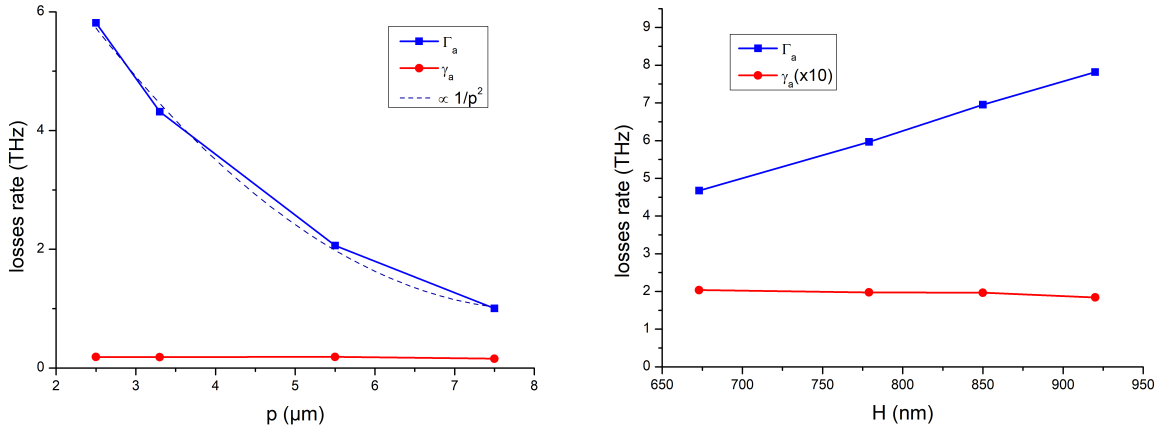
(b) Efficiency at the varying of p ($s = 1.3 \mu\text{m}$).

Figure 4.8: Absorption efficiency for different values of s and p obtained through FEM simulation and computed with the CMT approach.

Concerning the losses, it is interesting to study how they are affected by the geometry of the device, and in particular by the patch-period and the cavity thickness. The results in Figure 4.9 have been obtained varying these two geometrical features, with $p = 2.5 \mu\text{m}/3.3 \mu\text{m}/5.5 \mu\text{m}/7.5 \mu\text{m}$ and $H = 673 \text{ nm}/779 \text{ nm}/850 \text{ nm}/920 \text{ nm}$. The behaviour of the losses fits with the expectations deriving from CMT and the previous analysis on the empty cavities. In particular, the decay of the radiative losses with larger p follows a quadratic law, as remarked by the dashed line in Figure 4.9a, whereas the non-radiative ones are not significantly modified. However, since the previous experimental analysis has revealed that the FEM simulation tends to underestimate the non-radiative losses, their actual value is expected to be larger and increasing with the array periodicity.

On the other hand, the non-radiative losses rate is reduced for thicker cavities, as one can see in Figure 4.9b where γ_a is multiplied by a factor of 10 to improve the visibility of the trend. This result confirms that the dissipation in the gold layers is reduced when H is increased, as it has already been observed in the empty cavities, both experimentally and in the simulations.

The low values for the non-radiative losses rates derived from the reflectivity spectra of the simulations are due to the fact that despite the correction on the gold refractive index there are still non-idealities factors that have not been included. Hence, the actual non-radiative losses are expected to be higher than the ones obtained via simulations.



(a) Losses rates at the varying of p ($s = 1.3 \mu\text{m}$). The dashed line shows that Γ_a decays as p^{-2} .

(b) Losses rates at the varying of H ($s = 1.37 \mu\text{m}$, $p = 3.3 \mu\text{m}$), with γ_a magnified of a factor 10.

Figure 4.9: Radiative and non-radiative losses rates (Γ_a and γ_a) as a function of the period p and the cavity thickness H .

5 Conclusions and future perspectives

The analysis I carried out on these devices has highlighted the key geometrical parameters of the patch-antenna metamaterial. The FEM simulations have proven to be a valuable tool to evaluate the response of a certain configuration. Despite all the non-idealities that are present in the real system, it is possible to get a reasonable agreement with the experimental results by introducing a correction accounting for the defects in the fabrication process that induce a deviation from the theoretical behaviour. In particular, the gold refractive index has been modified with respect to the theoretical value [19] by using a fitting parameter in its dielectric function in order to match with experimental results. This approach allows to compensate for the imperfections present and acting as scattering centers, and also for the fact that in the real system the top metallic layer on the cavity is not made of pure gold, but actually of an alloy of Pd/Ge/Ti/Au.

The Coupled Mode Theory supplies the analytical model needed to relate the reflectivity, which can be found experimentally and via COMSOL simulations, to the losses, that cannot be directly observed but that are fundamental for the understanding of the system dynamics.

Finally, it has been shown that a decrease of the cavity thickness allows to lower the ohmic losses thanks to the reduced interaction of the cavity mode with the gold. However, such dimension has always to be smaller than the operating wavelength in order to preserve the confinement of the electric field in the cavity. Furthermore, increasing the array periodicity enables the critical coupling regime that is desired in order to maximise the absorption of the detector. This is possible by exploiting the super-radiance phenomenon where sparser arrays have lower radiative losses.

The understanding of light-matter interaction and the dynamical evolution in these structures lay the foundation for a further improvement, that is the possibility of integrating multiple functions besides detection, such as emission or modulation. A careful band engineering is necessary in order to obtain a bifunctional active medium behaving as a laser when a bias is applied and as a detector when in photovoltaic regime. A bifunctional Quantum Cascade Laser/Detector can be implemented so that lasing performances are not deteriorated by the additional detecting function [23].

The combination of the performances enhancement obtained with the patch-antenna metamaterial and an adequate design of the active region can lead to the implementation of integrated photonics that can find application for extremely compact devices useful for chemical sensing or telecommunications.

References

- [1] Azzurra Bigioli. “Uncooled unipolar receivers for 9 μm wavelength heterodyne detection”. PhD thesis. Université de Paris, Feb. 2021.
- [2] Christopher A. Curwen, John L. Reno, and Benjamin S. Williams. “Broadband continuous single-mode tuning of a short-cavity quantum-cascade VECSEL”. In: *Nature Photonics* 13.12 (Dec. 2019), pp. 855–859. ISSN: 1749-4893. DOI: 10.1038/s41566-019-0518-z.
- [3] Joel Pérez-Urquizo et al. “Monolithic Patch-Antenna THz Lasers with Extremely Low Beam Divergence and Polarization Control”. In: *ACS Photonics* 8.2 (2021), pp. 412–417. DOI: 10.1021/acsp Photonics.0c01430.
- [4] Daniele Palaferri et al. “Room-temperature nine- μm -wavelength photodetectors and GHz-frequency heterodyne receivers”. In: *Nature* 556.7699 (Apr. 2018), pp. 85–88. ISSN: 1476-4687. DOI: 10.1038/nature25790.
- [5] Azzurra Bigioli et al. “Long-wavelength infrared photovoltaic heterodyne receivers using patch-antenna quantum cascade detectors”. In: *Applied Physics Letters* 116.16 (2020), p. 161101. DOI: 10.1063/5.0004591.
- [6] Mathieu Jeannin et al. “Absorption Engineering in an Ultrasubwavelength Quantum System”. In: *Nano Letters* 20.6 (2020). PMID: 32407632, pp. 4430–4436. DOI: 10.1021/acs.nanolett.0c01217.
- [7] K.F. Lee, K.M. Luk, and H.W. Lai. *Microstrip Patch Antennas*. World Scientific Publishing Company Pte. Limited, 2018. ISBN: 9789813208599.
- [8] Constantine A. Balanis. *Antenna Theory: Analysis and Design*. (cit. on pp. 46, 50, V–VII). John Wiley & Sons, 2016. ISBN: 978-1-118-64206-1.
- [9] Mandar P. Joshi and Vitthal J. Gond. “Microstrip patch antennas for wireless communication: A review”. In: *2017 International Conference on Trends in Electronics and Informatics (ICEI)*. 2017, pp. 96–99. DOI: 10.1109/ICEI.2017.8300853.
- [10] Daniele Palaferri. “Antenna resonators for quantum infrared detectors and fast heterodyne receivers”. PhD thesis. Université Sorbonne Paris Cité, Feb. 2018.
- [11] Y. Todorov et al. “Ultrastrong Light-Matter Coupling Regime with Polariton Dots”. In: *Phys. Rev. Lett.* 105 (19 Nov. 2010), p. 196402. DOI: 10.1103/PhysRevLett.105.196402.
- [12] Y. Todorov et al. “Polaritonic spectroscopy of intersubband transitions”. In: *Phys. Rev. B* 86 (12 Sept. 2012), p. 125314. DOI: 10.1103/PhysRevB.86.125314. URL: <https://link.aps.org/doi/10.1103/PhysRevB.86.125314>.
- [13] Tie Jun Cui et al. “Coding metamaterials, digital metamaterials and programmable metamaterials”. In: *Light: Science & Applications* 3.10 (Oct. 2014), e218–e218. ISSN: 2047-7538. DOI: 10.1038/lsa.2014.99.
- [14] James Grant et al. “Polarization insensitive, broadband terahertz metamaterial absorber”. In: *Opt. Lett.* 36.17 (Sept. 2011), pp. 3476–3478. DOI: 10.1364/OL.36.003476.

- [15] Konstantinos Pantzas. Research Scientist, CNRS Center for Nanostructures and Nanosciences.
- [16] Daniel Hofstetter et al. In: *Applied Physics Letters* 81 (2002).
- [17] Mathieu Jeannin et al. “Ultrastrong Light–Matter Coupling in Deeply Subwavelength THz LC Resonators”. In: *ACS Photonics* 6.5 (May 2019), pp. 1207–1215. DOI: 10.1021/acsp Photonics.8b01778.
- [18] Sadao Adachi. “Optical dispersion relations for GaP, GaAs, GaSb, InP, InAs, InSb, Al_xGa_{1-x}As, and In_{1-x}Ga_xAs_yP_{1-y}”. In: *Journal of Applied Physics* 66.12 (1989), pp. 6030–6040. DOI: 10.1063/1.343580.
- [19] Mark A. Ordal et al. “Optical properties of Au, Ni, and Pb at submillimeter wavelengths”. In: *Appl. Opt.* 26.4 (Feb. 1987), pp. 744–752. DOI: 10.1364/AO.26.000744.
- [20] Anastasiya Derkachova, Krystyna Kolwas, and Iraida Demchenko. “Dielectric Function for Gold in Plasmonics Applications: Size Dependence of Plasmon Resonance Frequencies and Damping Rates for Nanospheres”. eng. In: *Plasmonics (Norwell, Mass.)* 11 (2016). 128[PII], pp. 941–951. ISSN: 1557-1955. DOI: 10.1007/s11468-015-0128-7.
- [21] M. A. Ordal et al. “Optical properties of fourteen metals in the infrared and far infrared: Al, Co, Cu, Au, Fe, Pb, Mo, Ni, Pd, Pt, Ag, Ti, V, and W.” In: *Appl. Opt.* 24.24 (Dec. 1985), pp. 4493–4499. DOI: 10.1364/AO.24.004493.
- [22] H.A. Haus and J.R. Melcher. *Electromagnetic Fields and Energy*. Prentice Hall, 1989. ISBN: 9780132492775.
- [23] Benedikt Schwarz et al. “Watt-Level Continuous-Wave Emission from a Bifunctional Quantum Cascade Laser/Detector”. In: *ACS Photonics* 4.5 (2017), pp. 1225–1231. DOI: 10.1021/acsp Photonics.7b00133.